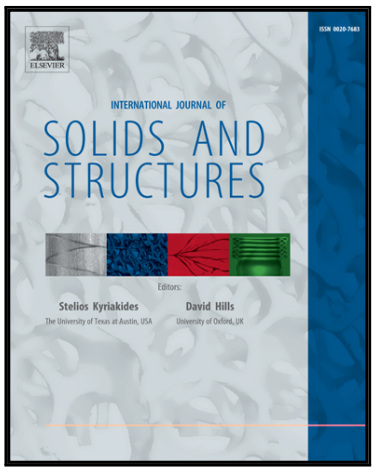

Inversion of point-like scatterers in an elastic half-space by the application of the far-field properties of the Green's function to the near-field operator

Terumi Touhei

PII: S0020-7683(17)30545-0
DOI: 10.1016/j.ijsolstr.2017.12.009
Reference: SAS 9827

To appear in: *International Journal of Solids and Structures*

Received date: 24 September 2017
Accepted date: 8 December 2017

Please cite this article as: Terumi Touhei, Inversion of point-like scatterers in an elastic half-space by the application of the far-field properties of the Green's function to the near-field operator, *International Journal of Solids and Structures* (2017), doi: 10.1016/j.ijsolstr.2017.12.009

Inversion of point-like scatterers in an elastic half-space by the application of the far-field properties of the Green's function to the near-field operator

Terumi Touhei *

Abstract

This article presents a method for reconstruction of the locations of point-like scatterers in an elastic half-space. The key point of the formulation is to introduce the far-field properties of the Green's function into the near field equation by means of pseudo projections, which are defined in this article. An indicator function that reconstructs the locations of the point-like scatterers was defined based on the derived operator. Numerical calculations were carried out to verify the accuracy of the pseudo-projection method. We also examined the effects of random noise, the grid resolution at the free surface, and the analyzed frequency on the accuracy of the reconstruction of scatterer locations.

Key words: inverse scattering problem, point-like scatterers, elastic half-space, far-field properties of Green's function, near-field equation, pseudo projections

*Dept. of Civil Engineering, Tokyo University of Science, 2641 Yamazaki, Noda 278-8510, Japan
e-mail touhei@rs.noda.tus.ac.jp

1 INTRODUCTION

Inverse scattering analysis has a long history due to its inherent appeal as well as applications such as geophysical exploration, site characterization, medical imaging, and nondestructive testing. During the past two decades or more, many significant articles in this field have been published. For example, Colton and Kress (1998) surveyed and reported a vast number of articles on inverse scattering analysis. Pelekanos, Abubakar, and van den Berg (2004) presented a contrast source inversion method in a two-dimensional (2D) elastic wavefield. Abubakar et al. (2011) developed a method for coupling the full-waveform inversion and the finite difference source-contrast method for a three-dimensional (3D) acoustic wavefield. Romdhane, Brossier, Réjiba, et al. (2011) also applied a 2D full-waveform inversion to a shallow structure with complex topography.

In contrast to the full-waveform inversion, linear sampling and factorization methods can reconstruct the support of scattering objects when the type of boundary condition is unknown. The linear sampling method was first presented by Colton and Kirsch (1996) for the 2D Helmholtz equation. They proved the divergence properties of the solution of the far-field equation, from which they reconstructed the support of a scattering object. Kirsch (2011) also developed a method to examine the range of the far-field operator for the 2D Helmholtz equation by the factorization of the operator, and presented an indicator function to reconstruct the supports of scattering objects.

After Colton and Kirsch (1996), Fata and Guzina (2004) developed a linear sampling method for an elastic half-space by means of the near-field equation. They also gave the mathematical details of the divergence properties of the near-field equation for cavi-

ties, rigid inclusions, or both. Baganas, Guzina, Charalambopoulos, and Manolis (2006) extended the method of the near-field equation for an elastic half-space to the interior transmission problem. Guzina and Madyarov (2007) carried out a reconstruction of scatterers in piecewise-homogeneous domains by linear sampling. Pourahmadian, Guzina, and Haddar (2017) presented a generalized linear sampling method for the reconstruction of heterogeneous fractures. The factorization method is also a useful tool for elastic wave scattering problems. For example, Gintides, Sini, and Thành (2011) applied the method to reconstruct point-like scatterers in 2D full-space by using one type of elastic scattering waves (P or S waves).

The authors' research group also applied a linear sampling approach to evaluate the location and spatial spread of fluctuations (Touhei, Fukushiro, and Tanaka 2015). The authors' method showed that the concept of the solvability index worked well even for scattered fluctuations in an elastic half-space. The locations and number of sources and the resolution of the observation grid, however, significantly influenced the accuracy of the reconstruction.

In this article, to resolve the stability of our linear sampling method, the far-field properties of the Green's function for an elastic half-space are incorporated into the near-field equation. The far-field properties of the Green's function are derived by applying the steepest descent path method. The pseudo projections are derived from the far-field properties of the Green's function, which is applied to the near-field operator. Since the pseudo projections are defined with respect to each probing point, the range of the derived far-field operator also depends on the location of the probing point. In spite of

the complicated procedure, it is expected to improve the accuracy of the reconstruction due to the analysis of the range of the operator with respect to each probing point. In this article, the discussion starts with the definition and formulation of the problem in the next section.

2 Theoretical Formulation

2.1 Definition of the scattering problem and basic equations

Figure 1 shows the concept of the wave problem dealt with here. The wavefield is a 3D elastic half-space, in which the incident waves from point sources at the free surface propagate toward the scattering objects embedded in the half-space, and the waves are scattered back to the free surface where we can observe them. The challenge here is to develop a method to identify the locations of the scattering objects by means of a far-field operator derived from near-field observations.

The analysis is carried out in the frequency domain with a time factor of $\exp(-i\omega t)$, where ω is the circular frequency and t is time. For simplicity, the scattering objects are assumed to be sets of point-like scatterers. The Born approximation is employed to express the scattered wavefield. As shown in Fig. 1, the free surface of the elastic half-space is denoted by S and the interior region that includes the point-like scatterers is denoted by E. The number of source and observation points in S is finite. Let the set of source and observation points be denoted by

$$S_g = \{\vec{x}_p\}_{p=1}^{N} \subset S \tag{1}$$

where N is the number of points in S_g. Note that the source points are also used as

observation points in this article. The Green's function for the elastic half-space is denoted by $G_{ij}(\vec{x}, \vec{y})$, where the subscripts i and j describe the components of the Cartesian coordinate system, $\vec{x}$ is the field point, and $\vec{y}$ is the source point. (In this article, the Cartesian coordinate system is used unless otherwise stated.) The components of the spatial point in terms of Cartesian coordinates are expressed as

$$\vec{x} = (x_1, x_2, x_3) \in \mathbb{R}^2 \times \mathbb{R}_+ = \mathbb{R}^3_+ \tag{2}$$

where x_3 denotes the vertical coordinate with the positive direction downwards and $x_3 = 0$ denotes the free surface of the elastic half-space. The summation convention is assumed for the index subscripts.

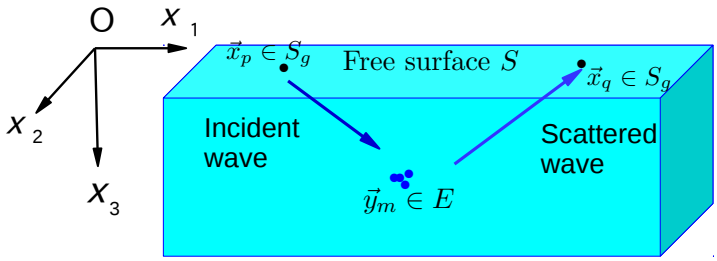

Figure 1: Concept of the scattering problem. An incident wave caused by a point source propagates to point-like scatterers. We observe the scattered waves at the free surface.

Green's function notations such as $G_{ij}^{E \swarrow S}(\vec{y}, \vec{x})$ and $G_{ij}^{S \nwarrow E}(\vec{x}, \vec{y})$, where $(\vec{x} \in S, \vec{y} \in E)$, are used for convenience in this article. These represent the waves that propagate from the free surface to the scattering objects and from the scattering objects to the free surface,

respectively. According to the reciprocity of the Green's function, they have the following relationship:

$$G_{ij}^{S\nwarrow E}(\vec{x},\vec{y}) = G_{ji}^{E\swarrow S}(\vec{y},\vec{x}), \quad \vec{x}\in S,\ \vec{y}\in E \tag{3}$$

The Green's function for an elastic half-space is defined by the following equation:

$$L_{ij}(\partial_1,\partial_2,\partial_3)G_{jk}(\vec{x},\vec{y}) = -\delta_{ik}\delta(\vec{x}-\vec{y}), \quad (\vec{x},\vec{y}\in\mathbb{R}^3_+) \tag{4}$$

$$\lim_{x_3\to 0} P_{ij}(\partial_1,\partial_2,\partial_3)G_{ij}(\vec{x},\vec{y}) = 0 \tag{5}$$

where L_{ij} is the Lamé operator defined by

$$L_{ij}(\partial_1,\partial_2,\partial_3) = (\lambda+\mu)\partial_i\partial_j + \delta_{ij}(\mu\partial_k\partial_k + \rho\omega^2) \tag{6}$$

and P_{ij} is an operator that transforms the displacement field to the traction for the x_3 plane, whose components are

$$\Big[P_{ij}(\partial_1,\partial_2,\partial_3)\Big] = \begin{bmatrix} \mu\partial_3 & 0 & \mu\partial_1 \\ 0 & \mu\partial_3 & \mu\partial_2 \\ \lambda\partial_1 & \lambda\partial_2 & (\lambda+2\mu)\partial_3 \end{bmatrix} \tag{7}$$

Note that λ and μ in Eqs. (6) and (7) are the Lamé constants and ρ in Eq. (6) is the mass density. In addition, δ_{ij} and $\delta(\cdot)$ in Eq. (4) are the Kronecker delta and Dirac delta function, respectively. The P and S wave velocities are denoted by c_α and c_β, respectively, which are obtained from

$$c_\alpha = \sqrt{(\lambda+2\mu)/\rho}, \quad c_\beta = \sqrt{\mu/\rho} \tag{8}$$

The wavenumbers for the P and S waves are expressed as

$$\xi_\alpha = \omega/c_\alpha,\ \xi_\beta = \omega/c_\beta \tag{9}$$

In this discussion, there are some cases in which we use notations such as β_V and β_H for expressing SV and SH waves, respectively. For example, we sometimes use ξ_{β_V} and ξ_{β_H}

for the wavenumber of SV and SH waves, respectively. Regardless of the notation, we understand that

$$\xi_\beta = \xi_{\beta_V} = \xi_{\beta_H} \tag{10}$$

2.2 Application of the steepest descent path method to the wavenumber integral representation of the Green's function

As is discussed in the **Appendix**, The Green's function for an elastic half-space can be expressed in terms of the wavenumber integral as follows:

$$G_{ij}^{S \nwarrow E}(\vec{x}, \vec{y}) = \frac{1}{2\pi} \sum_{m=-1}^{1} C_{ik}(\varphi) \int_0^\infty \xi h_{kl}^{(m)}(\xi : r, \varphi) g_{ln}(\xi : y_3) d\xi \, f_{nj}^{(m)} \quad (\vec{x} \in S, \vec{y} \in E) \tag{11}$$

where ξ is the radial wavenumber used for the parameter of the integral; m is the circumferential order; r and φ are the horizontal range and angle, respectively, determined by the component of $\vec{x}$ and $\vec{y}$ as shown in Fig. 2; C_{ik} transforms the cylindrical coordinate system to the Cartesian system; h_{kl} describes the horizontal wave propagation; g_{ln} is the Green's function in the wavenumber domain; and $f_{nj}^{(m)}$ denotes the effects of the point source in the wavenumber domain. The above variables used for the Green's function are further defined and clarified in the **Appendix**. Note that the summation convention is also applied to the index subscripts on the right side of Eq. (11), in spite of the fact that these subscripts may not be Cartesian coordinates.

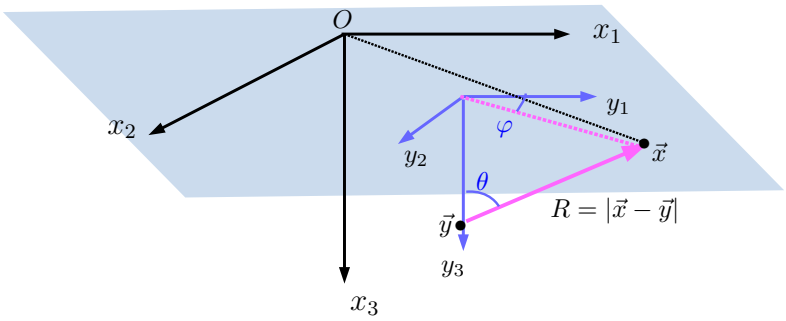

Figure 2: Definition of the angles θ and φ. These angles are determined by the relationship between $\vec{x}$ and $\vec{y}$. Note that R is the distance between $\vec{x}$ and $\vec{y}$, and it is used for the asymptotic form of the Green's function.

The far-field properties of the Green's function can be derived from the application of the steepest descent path method to Eq. (11). The procedure for the application of this method is given in the **Appendix**, from which we obtain the following results:

$$\begin{aligned} G_{ij}^{S^\kappa \diagdown E}(\vec{x},\vec{y}) \;=\; & \frac{e^{i\xi_\alpha|\vec{x}|}}{4\pi|\vec{x}|}\exp(-i\xi_\alpha \hat{x}\cdot\vec{y}) D_{ij}^{S^\kappa \diagdown E(\infty,\alpha)}(\theta,\varphi) \\ & + \frac{e^{i\xi_\beta|\vec{x}|}}{4\pi|\vec{x}|}\exp(-i\xi_\beta \hat{x}\cdot\vec{y}) D_{ij}^{S^\kappa \diagdown E(\infty,\beta_V)}(\theta,\varphi) \\ & + \frac{e^{i\xi_\beta|\vec{x}|}}{4\pi|\vec{x}|}\exp(-i\xi_\beta \hat{x}\cdot\vec{y}) D_{ij}^{S^\kappa \diagdown E(\infty,\beta_H)}(\theta,\varphi) \\ & + o(|\vec{x}|^{-1}), \quad \text{when } |\vec{x}| >> |\vec{y}| \end{aligned} \tag{12}$$

where $\hat{x} = \vec{x}/|\vec{x}|$, θ is the angle defined by

$$\theta = \sin^{-1}(y_3/R) \tag{13}$$

where $R = |\vec{x} - \vec{y}|$, which is shown in Fig. 2, and $D_{ij}^{S^{\kappa}\!\!\setminus E(\infty,\alpha)}(\theta,\varphi)$, $D_{ij}^{S^{\kappa}\!\!\setminus E(\infty,\beta_V)}(\theta,\varphi)$, and $D_{ij}^{S^{\kappa}\!\!\setminus E(\infty,\beta_H)}(\theta,\varphi)$ are the directivity tensors, respectively, for the P, SV, and SH waves from an interior point source $\vec{y}$ to the field point $\vec{x}$ at the free surface. Note that (θ,φ) describes the direction of wave propagation from the source point to the field point. We ignore the contribution of the Rayleigh and head waves in Eq. (12). The source point is deep enough from the free surface so that the Rayleigh effects are very small, as discussed in the **Appendix**. In addition, we know that the attenuation of the head wave is higher than $o(|\vec{x}|^{-1})$ (for example, Aki and Richards, 2002).

Straightforward calculations using Eq. (A.21) yield

$$
\begin{aligned}
\left[D_{ij}^{S^{\kappa}\!\!\setminus E(\infty,\alpha)}(\theta,\varphi)\right] &= 2\begin{bmatrix} g_{22}^{(\alpha)}(\xi_{s\alpha})\cos^2\varphi & g_{22}^{(\alpha)}(\xi_{s\alpha})\cos\varphi\sin\varphi & ig_{21}^{(\alpha)}(\xi_{s\alpha})\cos\varphi \\ g_{22}^{(\alpha)}(\xi_{s\alpha})\cos\varphi\sin\varphi & g_{22}^{(\alpha)}(\xi_{s\alpha})\sin^2\varphi & ig_{21}^{(\alpha)}(\xi_{s\alpha})\sin\varphi \\ -ig_{12}^{(\alpha)}(\xi_{s\alpha})\cos\varphi & -ig_{12}^{(\alpha)}(\xi_{s\alpha})\sin\varphi & g_{11}^{(\alpha)}(\xi_{s\alpha}) \end{bmatrix} \\
\left[D_{ij}^{S^{\kappa}\!\!\setminus E(\infty,\beta_V)}(\theta,\varphi)\right] &= 2\begin{bmatrix} g_{22}^{(\beta)}(\xi_{s\beta})\cos^2\varphi & g_{22}^{(\beta)}(\xi_{s\beta})\cos\varphi\sin\varphi & ig_{21}^{(\beta)}(\xi_{s\beta})\cos\varphi \\ g_{22}^{(\beta)}(\xi_{s\beta})\cos\varphi\sin\varphi & g_{22}^{(\beta)}(\xi_{s\beta})\sin^2\varphi & ig_{21}^{(\beta)}(\xi_{s\beta})\sin\varphi \\ -ig_{12}^{(\beta)}(\xi_{s\beta})\cos\varphi & -ig_{12}^{(\beta)}(\xi_{s\beta})\sin\varphi & g_{11}^{(\beta)}(\xi_{s\beta}) \end{bmatrix} \\
\left[D_{ij}^{S^{\kappa}\!\!\setminus E(\infty,\beta_H)}(\theta,\varphi)\right] &= 2\begin{bmatrix} \sin^2\varphi & -\cos\varphi\sin\varphi & 0 \\ -\cos\varphi\sin\varphi & \cos^2\varphi & 0 \\ 0 & 0 & 0 \end{bmatrix} g_{33}^{(\beta)}(\xi_{s\beta})
\end{aligned} \tag{14}
$$

where $\xi_{s\alpha}$ and $\xi_{s\beta}$ are the saddle points for the P and S waves, respectively, which are given by

$$\xi_{s\alpha} = \xi_{\alpha}\sin\theta \tag{15}$$

$$\xi_{s\beta} = \xi_{\beta}\sin\theta \tag{16}$$

and $g_{ij}^{(\alpha)}$ and $g_{ij}^{(\beta)}$ are the components of the Green's function in the wavenumber domain for the P and S waves, respectively, given in Eq. (A.7) in the **Appendix**. Equations (14) and (A.7) yield the decomposition of the directivity tensors for the P, SV, and SH waves

into the vector products, as in the following forms:

$$\begin{aligned} D_{ij}^{S^{\kappa}\!\!\searrow E(\infty,\alpha)}(\theta,\varphi) &= A^{(\alpha)}(\theta)W_i^{(\alpha)}(\theta,\varphi)V_j^{(\alpha)}(\theta,\varphi) \\ D_{ij}^{S^{\kappa}\!\!\searrow E(\infty,\beta_V)}(\theta,\varphi) &= A^{(\beta_V)}(\theta)\, W_i^{(\beta_V)}(\theta,\varphi)V_j^{(\beta_V)}(\theta,\varphi) \\ D_{ij}^{S^{\kappa}\!\!\searrow E(\infty,\beta_H)}(\theta,\varphi) &= A^{(\beta_H)}(\theta)V_i^{(\beta_H)}(\varphi)V_j^{(\beta_H)}(\varphi) \end{aligned} \tag{17}$$

where $V_i^{(\alpha)}$, $V_i^{(\beta_V)}$, and $V_i^{(\beta_H)}$ are the directions of vibrations for the P, SV, and SH waves in full space, respectively, and $W_i^{(\alpha)}$ and $W_i^{(\beta_V)}$ are the directions of the vibration of the P and SV waves at the free surface, respectively. The components of these vectors are defined by

$$\begin{aligned} \left(V_i^{(\alpha)}(\theta,\varphi)\right) &= \begin{pmatrix} \cos\varphi\sin\theta & \sin\varphi\sin\theta & \cos\theta \end{pmatrix} \\ \left(V_i^{(\beta_V)}(\theta,\varphi)\right) &= \begin{pmatrix} \cos\varphi\cos\theta & \sin\varphi\cos\theta & -\sin\theta \end{pmatrix} \\ \left(V_i^{(\beta_H)}(\varphi)\right) &= \begin{pmatrix} \sin\varphi & -\cos\varphi & 0 \end{pmatrix} \end{aligned} \tag{18}$$

$$\begin{aligned} \left(W_i^{(\alpha)}(\theta,\varphi)\right) &= \begin{pmatrix} \cos\varphi\sin\theta & \sin\varphi\sin\theta & \left(ig_{12}^{(\alpha)}(\theta)/g_{22}^{(\alpha)}(\theta)\right)\sin\theta \end{pmatrix} \\ \left(W_i^{(\beta_V)}(\theta,\varphi)\right) &= \begin{pmatrix} \cos\varphi\cos\theta & \sin\varphi\cos\theta & \left(ig_{12}^{(\beta)}(\theta)/g_{22}^{(\beta)}(\theta)\right)\cos\theta \end{pmatrix} \end{aligned} \tag{19}$$

In addition, $A^{(\alpha)}(\theta)$, $A^{(\beta_V)}$, and $A^{(\beta_H)}$ in Eq. (17) are given by

$$\begin{aligned} A^{(\alpha)}(\theta) &= \frac{2g_{22}^{(\alpha)}(\theta)}{\sin^2\theta} \\ A^{(\beta_V)}(\theta) &= \frac{2g_{22}^{(\beta)}(\theta)}{\cos^2\theta} \\ A^{(\beta_H)}(\theta) &= 2g_{33}^{(\beta)}(\theta) \end{aligned} \tag{20}$$

It is clear from Eq. (18) that

$$\begin{aligned} V_i^{(\alpha)}(\theta,\varphi)V_i^{(\beta_V)}(\theta,\varphi) &= V_i^{(\alpha)}(\theta,\varphi)V_i^{(\beta_H)}(\varphi) \\ &= V_i^{(\beta_V)}(\theta,\varphi)V_i^{(\beta_H)}(\varphi) \\ &= 0 \end{aligned} \tag{21}$$

which is the orthogonality relationship of the direction of the vibrations of the P, SV, and SH waves. On the other hand, we cannot establish the orthogonality relationship between the vibration directions of the P and SV waves at the free surface due to the interaction between the P and SV waves at the free surface. Namely,

$$W_i^{(\alpha)}(\theta,\varphi)W_i^{(\beta_V)}(\theta,\varphi) \neq 0 \tag{22}$$

According to the reciprocity of the Green's function, the far-field properties of $G_{ij}^{E\swarrow S}(\vec{y},\vec{x}), \vec{y} \in E, x \in S$ can be derived from Eq. (12), which is as follows:

$$\begin{aligned} G_{ij}^{E\swarrow S}(\vec{y},\vec{x}) &= \frac{e^{i\xi_\alpha|\vec{y}|}}{4\pi|\vec{y}|}\exp(-i\xi_\alpha\hat{y}\cdot\vec{x})D_{ij}^{E\swarrow S(\infty,\alpha)}(\theta,\varphi) \\ &\quad + \frac{e^{i\xi_\beta|\vec{y}|}}{4\pi|\vec{y}|}\exp(-i\xi_\beta\hat{y}\cdot\vec{x})D_{ij}^{E\swarrow S(\infty,\beta_V)}(\theta,\varphi) \\ &\quad + \frac{e^{i\xi_\beta|\vec{y}|}}{4\pi|\vec{y}|}\exp(-i\xi_\beta\hat{y}\cdot\vec{x})D_{ij}^{E\swarrow S(\infty,\beta_H)}(\theta,\varphi) \\ &\quad + o(|\vec{y}|^{-1}) \end{aligned} \tag{23}$$

where $\hat{y} = y/|\vec{y}|$. The decomposition of the directivity tensors into the vector products is given as

$$\begin{aligned} D_{ij}^{E\swarrow S(\infty,\alpha)}(\theta,\varphi) &= A^{(\alpha)}(\theta)V_i^{(\alpha)}(\theta,\varphi)W_j^{(\alpha)}(\theta,\varphi) \\ D_{ij}^{E\swarrow S(\infty,\beta_V)}(\theta,\varphi) &= A^{(\beta_V)}(\theta)\, V_i^{(\beta_V)}(\theta,\varphi)W_j^{(\beta_V)}(\theta,\varphi) \\ D_{ij}^{E\swarrow S(\infty,\beta_H)}(\theta,\varphi) &= A^{(\beta_H)}(\theta)V_i^{(\beta_H)}(\varphi)V_j^{(\beta_H)}(\varphi) \end{aligned} \tag{24}$$

Note that the angles θ and φ for Eq. (24) are determined by $\vec{x} \in S$ and $\vec{y} \in E$, which are explained in Fig. 2, so that these are identical for the use of Eq. (17).

2.3 Pseudo projection for the Green's function to extract the far-field pattern of one type of wave

At this point, we define the following vectors:

$$\begin{aligned} \left(W_i^{(\alpha\perp)}(\theta,\varphi)\right) &= \left(\cos\varphi \quad \sin\varphi \quad \left(ig_{22}^{(\alpha)}(\theta)/g_{12}^{(\alpha)}(\theta)\right) \right) \\ \left(W_i^{(\beta_V\perp)}(\theta,\varphi)\right) &= \left(\cos\varphi \quad \sin\varphi \quad \left(ig_{22}^{(\beta)}(\theta)/g_{12}^{(\beta)}(\theta)\right) \right) \end{aligned} \tag{25}$$

Then, we see that

$$\begin{aligned} W_i^{(\alpha\perp)}(\theta,\varphi)W_i^{(\alpha)}(\theta,\varphi) &= W_i^{(\beta_V\perp)}(\theta,\varphi)W_i^{(\beta_V)}(\theta,\varphi) \\ &= V_i^{(\beta_H)}(\varphi)W_i^{(\beta_V\perp)}(\theta,\varphi) \\ &= V_i^{(\beta_H)}(\varphi)W_i^{(\alpha\perp)}(\theta,\varphi) \\ &= 0 \end{aligned} \tag{26}$$

We also define the following matrices:

$$\begin{aligned} \mathcal{F}_{ij}^{(\alpha)}(\theta,\varphi) &= \frac{W_i^{(\alpha)}(\theta,\varphi)\, W_j^{(\beta_V\perp)}(\theta,\varphi)}{W_l^{(\alpha)}(\theta,\varphi)\, W_l^{(\beta_V\perp)}(\theta,\varphi)} \\ \mathcal{F}_{ij}^{(\beta_V)}(\theta,\varphi) &= \frac{W_i^{(\beta_V)}(\theta,\varphi)\, W_j^{(\alpha\perp)}(\theta,\varphi)}{W_l^{(\beta_V)}(\theta,\varphi)\, W_l^{(\alpha\perp)}(\theta,\varphi)} \\ \mathcal{F}_{ij}^{(\beta_H)}(\varphi) &= \frac{V_i^{(\beta_H)}(\varphi)\, V_j^{(\beta_H)}(\varphi)}{V_l^{(\beta_H)}(\varphi)\, V_l^{(\beta_H)}(\varphi)} \end{aligned} \tag{27}$$

Then, we have the following relationship between the above matrices:

$$\begin{aligned}\mathcal{F}_{ij}^{(\alpha)}(\theta,\varphi)\mathcal{F}_{jk}^{(\beta_V)}(\theta,\varphi) &= \mathcal{F}_{ij}^{(\beta_V)}(\theta,\varphi)\mathcal{F}_{jk}^{(\alpha)}(\theta,\varphi) = \mathcal{F}_{ij}^{(\alpha)}(\theta,\varphi)\mathcal{F}_{jk}^{(\beta_H)}(\varphi) \\ &= \mathcal{F}_{ij}^{(\beta_H)}(\varphi)\mathcal{F}_{jk}^{(\alpha)}(\theta,\varphi) = \mathcal{F}_{ij}^{(\beta_V)}(\theta,\varphi)\mathcal{F}_{jk}^{(\beta_H)}(\varphi) \\ &= \mathcal{F}_{ij}^{(\beta_H)}(\varphi)\mathcal{F}_{jk}^{(\beta_V)}(\theta,\varphi) = 0 \end{aligned} \tag{28}$$

$$\begin{aligned}\mathcal{F}_{ij}^{(\alpha)}(\theta,\varphi)\mathcal{F}_{jk}^{(\alpha)}(\theta,\varphi) &= \mathcal{F}_{ik}^{(\alpha)}(\theta,\varphi) \\ \mathcal{F}_{ij}^{(\beta_V)}(\theta,\varphi)\mathcal{F}_{jk}^{(\beta_V)}(\theta,\varphi) &= \mathcal{F}_{ik}^{(\beta_V)}(\theta,\varphi) \\ \mathcal{F}_{ij}^{(\beta_H)}(\varphi)\mathcal{F}_{jk}^{(\beta_H)}(\varphi) &= \mathcal{F}_{ik}^{(\beta_H)}(\varphi) \end{aligned} \tag{29}$$

Due to Eqs. (28) and (29), in spite of the fact that the matrices $\mathcal{F}_{ij}^{(\alpha)}$, $\mathcal{F}_{ij}^{(\beta_V)}$, and $\mathcal{F}_{ij}^{(\beta_H)}$ are not Hermitian, let us call them the pseudo projections. We can see the effects of the projections as follows:

$$\begin{aligned}\left(4\pi|\vec{x}|\right) e^{-i\xi_\alpha|\vec{x}|}\, \mathcal{F}_{ij}^{(\alpha)}(\theta,\varphi) G_{jk}^{S\nwarrow E}(\vec{x},\vec{y}) &= e^{-i\xi_\alpha \hat{x}\cdot\vec{y}}\, D_{ik}^{S\nwarrow E(\infty,\alpha)}(\theta,\varphi) \\ \left(4\pi|\vec{x}|\right) e^{-i\xi_\beta|\vec{x}|}\, \mathcal{F}_{ij}^{(\beta_V)}(\theta,\varphi) G_{jk}^{S\nwarrow E}(\vec{x},\vec{y}) &= e^{-i\xi_\beta \hat{x}\cdot\vec{y}}\, D_{ik}^{S\nwarrow E(\infty,\beta_V)}(\theta,\varphi) \\ \left(4\pi|\vec{x}|\right) e^{-i\xi_\beta|\vec{x}|}\, \mathcal{F}_{ij}^{(\beta_H)}(\varphi) G_{jk}^{S\nwarrow E}(\vec{x},\vec{y}) &= e^{-i\xi_\beta \hat{x}\cdot\vec{y}}\, D_{ik}^{S\nwarrow E(\infty,\beta_H)}(\theta,\varphi) \end{aligned} \tag{30}$$

$$\begin{aligned}\left(4\pi|\vec{y}|\right) e^{-i\xi_\alpha|\vec{y}|}\, G_{ij}^{E\swarrow S}(\vec{y},\vec{x})\, \mathcal{F}_{kj}^{(\alpha)}(\theta,\varphi) &= e^{-i\xi_\alpha \hat{y}\cdot\vec{x}}\, D_{ik}^{E\swarrow S(\infty,\alpha)}(\theta,\varphi) \\ \left(4\pi|\vec{y}|\right) e^{-i\xi_\beta|\vec{y}|}\, G_{ij}^{E\swarrow S}(\vec{y},\vec{x})\, \mathcal{F}_{kj}^{(\beta_V)}(\theta,\varphi) &= e^{-i\xi_\beta \hat{y}\cdot\vec{x}}\, D_{ik}^{E\swarrow S(\infty,\beta_V)}(\theta,\varphi) \\ \left(4\pi|\vec{y}|\right) e^{-i\xi_\beta|\vec{y}|}\, G_{ij}^{E\swarrow S}(\vec{y},\vec{x})\, \mathcal{F}_{kj}^{(\beta_H)}(\varphi) &= e^{-i\xi_\beta \hat{y}\cdot\vec{x}}\, D_{ik}^{E\swarrow S(\infty,\beta_H)}(\theta,\varphi) \end{aligned} \tag{31}$$

Thus, the matrices $\mathcal{F}_{ij}^{(\alpha)}$, $\mathcal{F}_{ij}^{(\beta_V)}$, and $\mathcal{F}_{ij}^{(\beta_H)}$ extract the far-field patterns for one type of wave (P, SV, or SH waves) from the Green's function.

2.4 Introduction of the far-field properties of the Green's function to the near-field operator

Now, let us return to the scattering problem shown in Fig. 1. Let $u_{ij}(\vec{x}_p, \vec{x}_q)$ be the scattered wave at the point $\vec{x}_p \in S_g$ for the i-th direction due to a unit point load for the j-th direction at the point $\vec{x}_q \in S_g$. When the Born approximation is employed, $u_{ij}(\vec{x}_p, \vec{x}_q)$ is expressed as

$$u_{ij}(\vec{x}_p, \vec{x}_q) = \sum_{\vec{y}_m \in E} G_{ik}^{S \nwarrow E}(\vec{x}_p, \vec{y}_m) Q_m G_{kj}^{E \swarrow S}(\vec{y}_m, \vec{x}_q), \quad (\vec{x}_p, \vec{x}_q \in S_g) \tag{32}$$

where Q_m is the strength of the point-like scatterers at $\vec{y}_m \in E$. The near-field operator is constructed by the stack $u_{ik}(\vec{x}_p, \vec{x}_q)$. Namely, we can define the near-field operator as the following finite dimensional linear transform:

$$\Big(U_{ij} f_k(\vec{x}_q)\Big)(\vec{x}_p) = \sum_{q=1}^{N} u_{ij}(\vec{x}_p, \vec{x}_q) f_k(\vec{x}_q), \quad (\vec{x}_p \in S_g) \tag{33}$$

where U_{ij} is the near-field operator. According to Eq. (32), Eq. (33) can be also expressed as

$$\begin{aligned} &\Big(U_{ij} f_j(\vec{x}_q)\Big)(\vec{x}_p) \\ &= \Big(\sum_{q=1}^{N} \sum_{\vec{y}_m \in E} G_{ik}^{S \nwarrow E}(\vec{x}_p, \vec{y}_m) Q_m G_{kj}^{E \swarrow S}(\vec{y}_m, \vec{x}_q)\Big) f_j(\vec{x}_q) \end{aligned} \tag{34}$$

The problem at this point is to introduce the far-field properties of the Green's function to the near-field operator shown in Eq. (34). Let us define the following matrix by means of the pseudo projections defined by Eq. (27):

$$\mathcal{P}_{ij}^{\#}(\vec{x}_p, \vec{z}_s) = 4\pi |\vec{x}_p - \vec{z}_s| e^{i\xi_{\#} |\vec{x}_p - \vec{z}_s|} \mathcal{F}_{ij}^{\#}\big(\theta_{(ps)}, \varphi_{(ps)}\big), \quad (\vec{z}_s \in B) \tag{35}$$

where # takes α, β_V or β_H, $\vec{z}_s$ is the probing grid location, and B is the set of the probing grid locations. Note that the angles $\theta_{(ps)}$ and $\varphi_{(ps)}$ are determined by the positions of $\vec{x}_p$ and $\vec{z}_s$, as shown in Fig. 3.

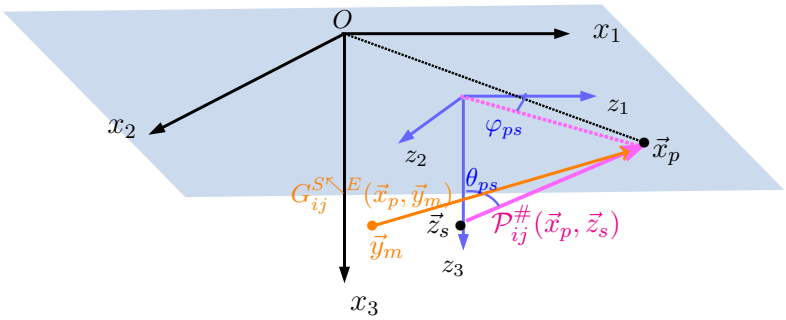

Figure 3: Path of waves for $G_{ij}^{S\nwarrow E}(\vec{x}_p, \vec{y}_m)$ and $\mathcal{P}_{ij}^{\#}(\vec{x}_p, \vec{z}_s)$, and definition of the angles $\theta_{(ps)}$ and $\varphi_{(ps)}$. Note that $\vec{z}_s$ is the probing point.

The operator $A_{ij}^{\infty\#}(\vec{z}_s)$ is the result of the introduction of the far-field properties of the Green's function into the near-field operator:

$$\left(A_{ij}^{\infty\#}(\vec{z}_s) f_j(\vec{x}_q)\right)(\vec{x}_p) = \sum_{q=1}^{N} \mathcal{P}_{ik}^{\#}(\vec{x}_p, \vec{z}_s) u_{kl}(\vec{x}_p, \vec{x}_q) \left(\mathcal{P}_{jl}^{\#}(\vec{x}_q, \vec{z}_s)\right)^T f_j(\vec{x}_q) \tag{36}$$

Incorporating Eqs. (33) and (34) into Eq. (36) yields

$$\begin{aligned} &\left(A_{ij}^{\infty\#}(\vec{z}_s) f_j(\vec{x}_q)\right)(\vec{x}_p) \\ &= \sum_{q=1}^{N} \sum_{\vec{y}_m \in E} T_{i\nu}^{\#}(\vec{x}_p, \vec{z}_s, \vec{y}_m)\, Q_m \left(T_{j\nu}^{\#}(\vec{x}_q, \vec{z}_s, \vec{y}_m)\right)^T f_j(\vec{x}_q) \end{aligned} \tag{37}$$

where

$$T^{\#}_{i\nu}(\vec{x}_p, \vec{z}_s, \vec{y}_m) = \mathcal{P}^{\#}_{ik}(\vec{x}_p, \vec{z}_s) G^{S\nwarrow E}_{k\nu}(\vec{x}_p, \vec{y}_m) \tag{38}$$

In Eq. (37), we have used the reciprocity of the Green's function:

$$\left(G^{S\nwarrow E}_{l\nu}(\vec{x}_q, \vec{z}_s)\right)^T = G^{E\swarrow S}_{\nu l}(\vec{z}_s, \vec{x}_q) \tag{39}$$

At this point, let us assume that

$$| \vec{x}_p - \vec{z}_s | >> | \vec{y}_m - \vec{z}_s |, \quad (\vec{x}_p \in S_g) \tag{40}$$

Then, we have

$$\frac{e^{i\xi_{\#}|\vec{x}_p - \vec{y}_m|}}{4\pi|\vec{x}_p - \vec{y}_m|} = \frac{e^{i\xi_{\#}|\vec{x}_p - \vec{z}_s|}}{4\pi|\vec{x}_p - \vec{z}_s|} \exp\left(-i\xi_{\#}\hat{d}_{(ps)} \cdot (\vec{z}_s - \vec{y}_m)\right) + o\Big(| \vec{x}_p - \vec{z}_s |^{-1}\Big) \tag{41}$$

where

$$\hat{d}_{(ps)} = \frac{\vec{x}_p - \vec{z}_s}{|\vec{x}_p - \vec{z}_s|} \tag{42}$$

and we see that

$$\begin{aligned}
&T^{\#}_{i\nu}(\vec{x}_p, \vec{z}_s, \vec{y}_m) \\
&= \mathcal{P}^{\#}_{ij}(\vec{x}_p, \vec{z}_s) G^{S\nwarrow E}_{jk}(\vec{x}_p, \vec{y}_m) \\
&= \exp(-i\xi_{\#}|\vec{x}_p - \vec{z}_s|) \mathcal{F}^{\#}_{ij}(\theta_{(ps)}, \varphi_{(ps)}) \\
&\quad \times \Big(\exp(i\xi_\alpha|\vec{x}_p - \vec{z}_s|)\ \exp\left(-i\xi_\alpha \hat{d}_{(ps)} \cdot (\vec{y}_m - \vec{z}_s)\right) D^{S\nwarrow E(\alpha)}_{jk}(\theta_{(ps)}, \varphi_{(ps)}) \\
&\qquad + \exp\left(i\xi_\beta|\vec{x}_p - \vec{z}_s|\right)\ \exp\left(-i\xi_\beta \hat{d}_{(ps)} \cdot (\vec{y}_m - \vec{z}_s)\right) D^{S\nwarrow E(\beta_V)}_{jk}(\theta_{(ps)}, \varphi_{(ps)}) \\
&\qquad + \exp\left(i\xi_\beta|\vec{x}_p - \vec{z}_s|\right)\ \exp\left(-i\xi_\beta \hat{d}_{(ps)} \cdot (\vec{y}_m - \vec{z}_s)\right) D^{S\nwarrow E(\beta_H)}_{jk}(\theta_{(ps)}, \varphi_{(ps)}) \Big)
\end{aligned} \tag{43}$$

Therefore, if there exists $\vec{y}_{m^*} \in E$ such that

$$\vec{y}_{m^*} = \vec{z}_s \tag{44}$$

then the following relationship can be derived:

$$T_{i\nu}^{\#}(\vec{x}_p, \vec{z}_s, \vec{y}_{m^*}) \;=\; D_{ik}^{S^{\kappa} \diagdown E(\infty,\#)}(\theta_{(ps)}, \varphi_{(ps)}) \tag{45}$$

As a result, we have

$$\begin{aligned}
&\Big(A_{ij}^{\infty\#}(\vec{z}_s) f_j(\vec{x}_q)\Big)(\vec{x}_p) \\
&= \sum_{q=1}^{N} \Big[D_{i\nu}^{S^{\kappa} \diagdown E(\infty,\#)}(\theta_{(ps)}, \varphi_{(ps)})\, Q_{m^*} \left(D_{j\nu}^{S^{\kappa} \diagdown E(\infty,\#)}(\theta_{(qs)}, \varphi_{(qs)}) \right)^T \\
&\qquad + \sum_{m \neq m^*} T_{i\nu}^{\#}(\vec{x}_p, \vec{z}_s, \vec{y}_m)\, Q_m \left(T_{j\nu}^{\#}(\vec{x}_p, \vec{z}_s, \vec{y}_m) \right)^T \Big]\, f_j(\vec{x}_q) \\
&= D_{i\nu}^{S^{\kappa} \diagdown E(\infty,\#)}(\theta_{(ps)}, \varphi_{(ps)}) b_\nu + X_i(\vec{x}_p)
\end{aligned} \tag{46}$$

where

$$\begin{aligned}
b_\nu \;&=\; Q_{m^*} \sum_{q=1}^{N} \Big(D_{j\nu}^{S^{\kappa} \diagdown E(\infty,\#)}(\theta_{(qs)}, \varphi_{(qs)}) \Big)^T f_j(\vec{x}_q) \\
X_i(\vec{x}_p) \;&=\; \sum_{q=1}^{N} \sum_{m \neq m^*} T_{i\nu}^{\#}(\vec{x}_p, \vec{z}_s, \vec{y}_m)\, Q_m \left(T_{j\nu}^{\#}(\vec{x}_p, \vec{z}_s, \vec{y}_m) \right)^T f_j(\vec{x}_q)
\end{aligned} \tag{47}$$

At this point, in order to characterize the range of the operator $A_{ij}^{(\infty,\#)}(\vec{z}_s)$, let us define the following vector for fixed index ν:

$$\begin{aligned}
&\boldsymbol{D}_{\nu}^{S^{\kappa} \diagdown E(\infty,\#)}(\theta_s, \varphi_s) \\
&= \Big(\big(D_{i\nu}^{S^{\kappa} \diagdown E(\infty\#)}(\theta_{(1s)}, \varphi_{(1s)}) \big), \big(D_{i\nu}^{S^{\kappa} \diagdown E(\#)}(\theta_{(2s)}, \varphi_{(2s)}) \big), \ldots, \big(D_{i\nu}^{S^{\kappa} \diagdown E(\#)}(\theta_{(Ns)}, \varphi_{(Ns)}) \big) \Big)^T
\end{aligned} \tag{48}$$

Note that $\left(D_{i\nu}^{S^{\kwedge}E(\infty\#)}(\theta_{(ps)},\varphi_{(ps)})\right)$ is also the array of

$$\begin{aligned}&\left(D_{i\nu}^{S^{\kwedge}E(\#)}(\theta_{(ps)},\varphi_{(ps)})\right)\\ &= \left(D_{1\nu}^{S^{\kwedge}E(\#)}(\theta_{(ps)},\varphi_{(ps)}), D_{2\nu}^{S^{\kwedge}E(\#)}(\theta_{(ps)},\varphi_{(ps)}), D_{3\nu}^{S^{\kwedge}E(\#)}(\theta_{(ps)},\varphi_{(ps)})\right)^T \end{aligned} \tag{49}$$

for $1 \leq p \leq N$. It is found from Eq. (46) and by means of the vector defined by Eq. (48) that the range of the operator $A_{ij}^{(\infty,\#)}(\vec{z}_s)$ can be expressed as follows:

$$\vec{z}_s \in \{\vec{y}_m\}_{\vec{y}_m \in E} \implies \boldsymbol{D}_k^{S^{\kwedge}E(\infty,\#)}(\theta_s,\varphi_s) \in \text{ran } A_{ij}^{(\infty,\#)}(\vec{z}_s) \tag{50}$$

2.5 Indicator functions for reconstructing the locations of point-like scatterers

We are now at the stage of presenting the indicator functions for reconstructing the locations of the point-like scatterers. Let $\ker\left(A_{ij}^{\infty\#}(\vec{z}_s)\right)^H$ be the kernel of the Hermitian adjoint of the operator $A_{ij}^{\infty\#}(\vec{z}_s)$. Then, we know the following relationship:

$$\ker\left(A_{ij}^{\infty\#}(\vec{z}_s)\right)^H \perp \text{ran } A_{ij}^{\infty\#}(\vec{z}_s) \tag{51}$$

Let $\{\boldsymbol{\Psi}_n^{\#}(\vec{z}_s)\}_n$ be the basis for $\ker\left(A_{ij}^{\infty\#}(\vec{z}_s)\right)^H$ and we define the following spatial function with respect to the probing point $\vec{z}_s$:

$$\phi^{\#}(\vec{z}_s) = \frac{1}{\sum_{\nu=1}^{3}\sum_n \left|\left(\boldsymbol{\Psi}_n^{\#}(\vec{z}_s)\right)^H \boldsymbol{D}_\nu^{S^{\kwedge}E(\infty,\#)}(\theta_s,\varphi_s)\right|^2} \tag{52}$$

Namely, we have three spatial functions $\phi^{\alpha}(\cdot)$, $\phi^{\beta_V}(\cdot)$, and $\phi^{\beta_H}(\cdot)$ for the P, SV, and SH waves, respectively. In the following numerical examples, we will also examine the indicator function:

$$\phi(\vec{z}_s) = \phi^{(\alpha)}(\vec{z}_s)\phi^{(\beta_V)}(\vec{z}_s)\phi^{(\beta_H)}(\vec{z}_s) \tag{53}$$

Note that the derived operator $A_{ij}^{\infty,\#}$ is defined with respect to each probing point. Therefore, the basis $\{\mathbf{\Psi}_n^{\#}(\vec{z}_s)\}_n$ has to also be defined for each probing point. This aspect increases the computational cost of our method. In spite of the situation, it is expected that the investigation of the range of the operator with respect to each probing point will enable us to carry out an accurate analysis. Discussions regarding the accuracy of the method, as well as the computational costs, are given in the next section.

3 Numerical Examples

3.1 Analysis model

The model we analyzed to verify our proposed formulation is shown in Figs. 4(a) and 4(b), which show planar and bird's eye views of the model, respectively. The grid interval at the free surface for the sources and observations is 0.5 km and the number of grid intersections, that is, source and observation points, is 121. The grid interval for the point-like scatterers is 250 m and the number of scatterers is 900. The set of point-like scatterers forms an object shape in an elastic half-space. The shape of the object in this numerical example is based on the shape described in Abubakar et al. (2011). For the material properties of the elastic half-space, the P and S wave velocities are 2 km/s and 1 km/s, respectively, and the mass density is 2.0 g/cm^3. We employed two probing planes that cross the scattering object horizontally and vertically, as shown in Fig. 5, to examine the properties of the indicator function defined in the theoretical formulations. The positions of these probing planes are $x_3 = 4.0$ km and $x_1 = 8.0$ km, respectively. The construction of the near-field operator for all of the numerical examples is based on the

wavenumber integral representation of the Green's function shown in Eq. (11).

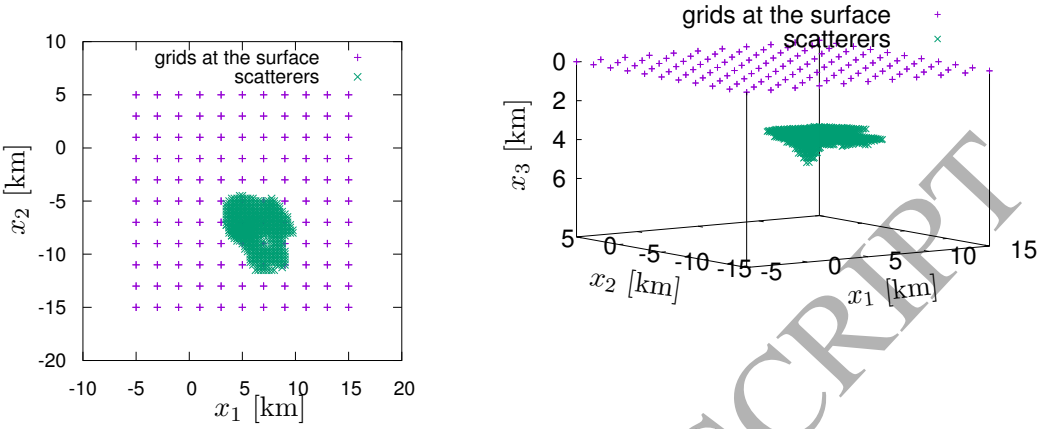

(a) Planar view (b) Bird's eye view

Figure 4: Analysis model showing the source-observation grid at the free surface and the set of point-like scatterers in the elastic half-space.

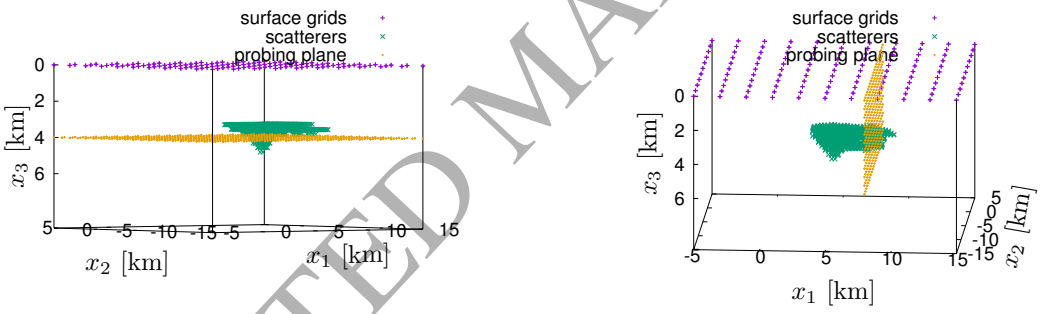

(a) Probing plane at x_3=4 [km] (b) Probing plane at $x_1 = 8$ [km]

Figure 5: Two probing planes that cross the scattering object horizontally and vertically.

3.2 Properties of the indicator functions with respect to wave types and their multiplication

As described in the previous section, we have three kinds of indicator functions $\phi^{\#}(\cdot)$ ($\# = \mathrm{P}, \mathrm{SV}, \mathrm{SH}$) for each type of wave and their multiplication $\phi(\cdot)$ as shown in Eq. (53). Here, we investigate the properties of these indicator functions as the first numerical

example in this article. Figures 6(a)-(d) and 7(a)-(d) show the spatial distributions of the amplitudes of the indicator functions on the horizontal and vertical probing planes, respectively. The point-like scatterers in the range $3.5 \leq x_3 \leq 4.5$ km are plotted in Fig. 6, and scatterers in the range $7.5 \leq x_1 \leq 8.5$ km are plotted in Fig. 7 to check the accuracy of the reconstruction results. The analyzed frequency is 1.0 Hz.

The plots in Fig. 6 show that the high-amplitude areas of the indicator functions agree well with the locations of the point-like scatterers. The spatial spreads and the amplitudes of the indicator functions differ slightly for the P, SV, and SH wave components. However, after multiplication, the reconstructed locations of the point-like scatters on the horizontal plane for these indicator functions have satisfactory accuracy.

In Fig. 7, the high-amplitude areas of the indicator functions in the vertical probing plane almost agree with the locations of the point-like scatterers. A closer look at the spatial distribution of the indicator functions, however, reveals differences in the spatial spreads of the high-amplitude areas for each wave type. Namely, the spatial spreads of the indicator functions for the P and SH waves cover a wider area compared to the locations of the scatterers. In addition, the spatial spread of the indicator function for the SV wave does not show clear contrast for the scatterers. The final results obtained from the multiplication of the P, SV, and SH wave components, however, yield good sharp results for the reconstruction of the scatterer locations.

The validity of our formulation is assured by the above results. At this point, we can conclude that multiplication of the indicator function for each wave component improves the accuracy of the reconstruction of the scatterer locations. For this reason, all following

numerical results are derived using Eq. (53).

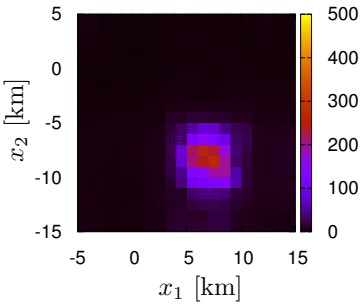

(a) P-wave component ϕ^{α}

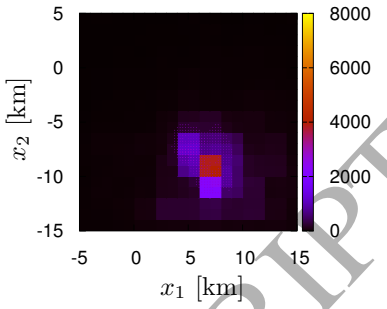

(b) SV-wave component ϕ^{β_V}

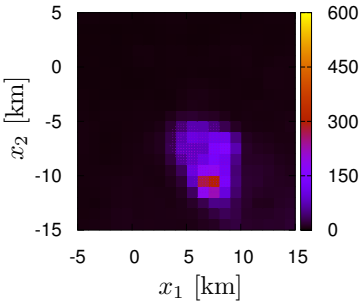

(c) SH-wave component ϕ^{β_H}

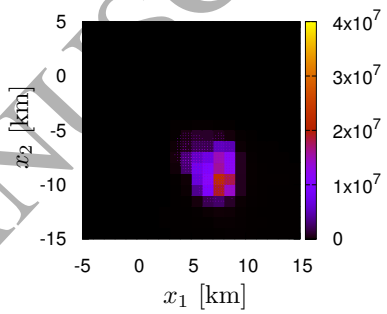

(d) Multiplication, $\phi = \phi^{\alpha}\phi^{\beta_V}\phi^{\beta_H}$

Figure 6: Spatial distribution of the indicator functions on the horizontal probing plane at $x_3 = 4.0$ km.

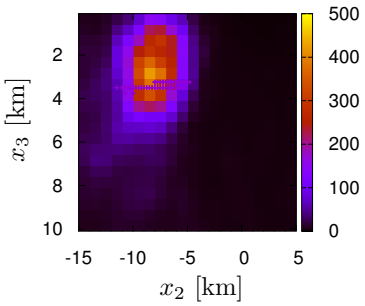

(a) P-wave component ϕ^{α}

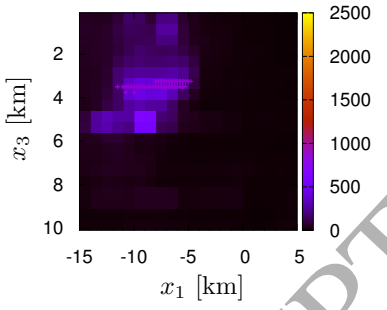

(b) SV-wave component ϕ^{β_V}

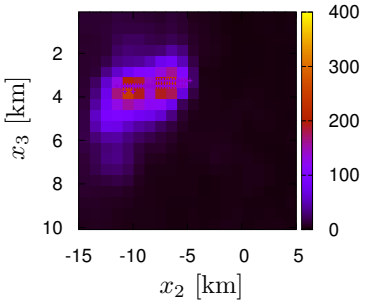

(c) SH-wave component ϕ^{β_H}

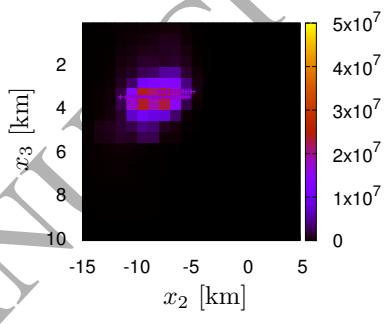

(d) Multiplication, $\phi = \phi^{\alpha}\phi^{\beta_V}\phi^{\beta_H}$

Figure 7: Spatial distribution of the indicator functions on the vertical probing plane at $x_1 = 8.0$ km.

3.3 Effect of random noise on the reconstruction of the locations of point-like scatterers

Let us apply random noise to the near-field operator and investigate the sensitivity of our method toward random noise. In the construction of the near-field operator as shown in Eq. (32), we use $G_{ij}^{S\nwarrow E}(\vec{x}_p, \vec{y}_m)$. Therefore, we apply random noise to this function, and instead of Eq. (32), we use

$$u_{ik}(\vec{x}_p, \vec{x}_q) = \sum_{\vec{y}_m \in E} \widetilde{G}_{ij}^{S\nwarrow E}(\vec{x}_p, \vec{y}_m) Q_m \widetilde{G}_{jk}^{E\swarrow S}(\vec{y}_m, \vec{x}_q) \tag{54}$$

where the Green's function $\widetilde{G}_{ij}^{S\nwarrow E}(\vec{x}_p, \vec{y}_m)$ with random noise is expressed as follows:

$$\widetilde{G}_{ij}^{S\nwarrow E}(\vec{x}_p, \vec{y}_m) = G_{ij}^{S\nwarrow E}(\vec{x}_p, \vec{y}_m) + \Delta_{ij}(\vec{x}_p, \vec{y}_m) \tag{55}$$

where Δ_{ij} is the random noise. Due to reciprocity, we assume that

$$\widetilde{G}_{jk}^{E\swarrow S}(\vec{y}_m, \vec{x}_q) = \widetilde{G}_{kj}^{S\nwarrow E}(\vec{x}_q, \vec{y}_m) \tag{56}$$

and as a result, Eq. (54) becomes possible. We also define the level of noise r_n as follows:

$$r_n^2 = \frac{\sum_{i=1}^{3}\sum_{j=1}^{3}\sum_{\vec{x}_p\in S_g}\sum_{\vec{y}_m\in E}|\Delta_{ij}(\vec{x}_p, \vec{y}_m)|^2}{\sum_{i=1}^{3}\sum_{j=1}^{3}\sum_{\vec{x}_p\in S_g}\sum_{\vec{y}_m\in E}|G_{ij}^{S\nwarrow E}(\vec{x}_p, \vec{y}_m)|^2} \tag{57}$$

Figures 8 and 9 show the effects of noise level r_n on the accuracy of the reconstructed locations of scatterers on the horizontal and vertical probing planes, respectively. The analyzed frequency is 1.0 Hz. When the noise level is 10%, the effects of the noise are not very significant for either the horizontal or vertical probing plane [Figs. 8(b) and 9(b), respectively]. The high-amplitude areas of the indicator functions almost agree with the locations of the scatterers. When the noise level is 15%, the accuracy of the reconstruction results is satisfactory for the horizontal probing plane [Fig. 8(c)]. On the other hand, the accuracy of the reconstruction results for the vertical probing plane decreases at this noise level. The high-amplitude areas of the indicator functions are found to deviate from the scatterer locations [Fig. 9(c)].

When the noise level is 20%, [Figs. 8(d) and 9(d)], the high-amplitude areas for the indicator functions do not agree well with the locations of the scatterers, especially on the vertical probing plane. Thus, if the noise level exceeds 20%, it is difficult to accurately reconstruct the scatterer locations.

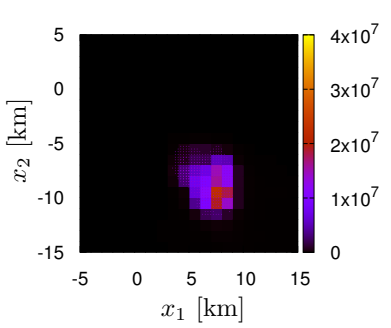

(a) Noise level 0%

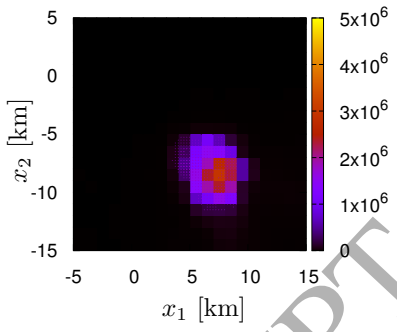

(b) Noise level 10%

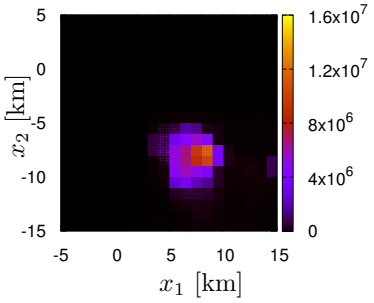

(c) Noise level 15%

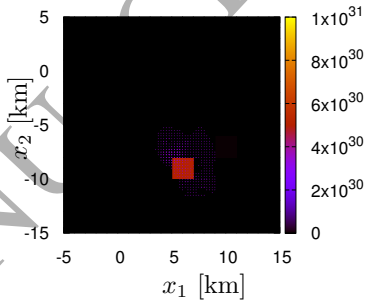

(d) Noise level 20%

Figure 8: Effects of random noise on the accuracy of the reconstruction for the horizontal probing plane

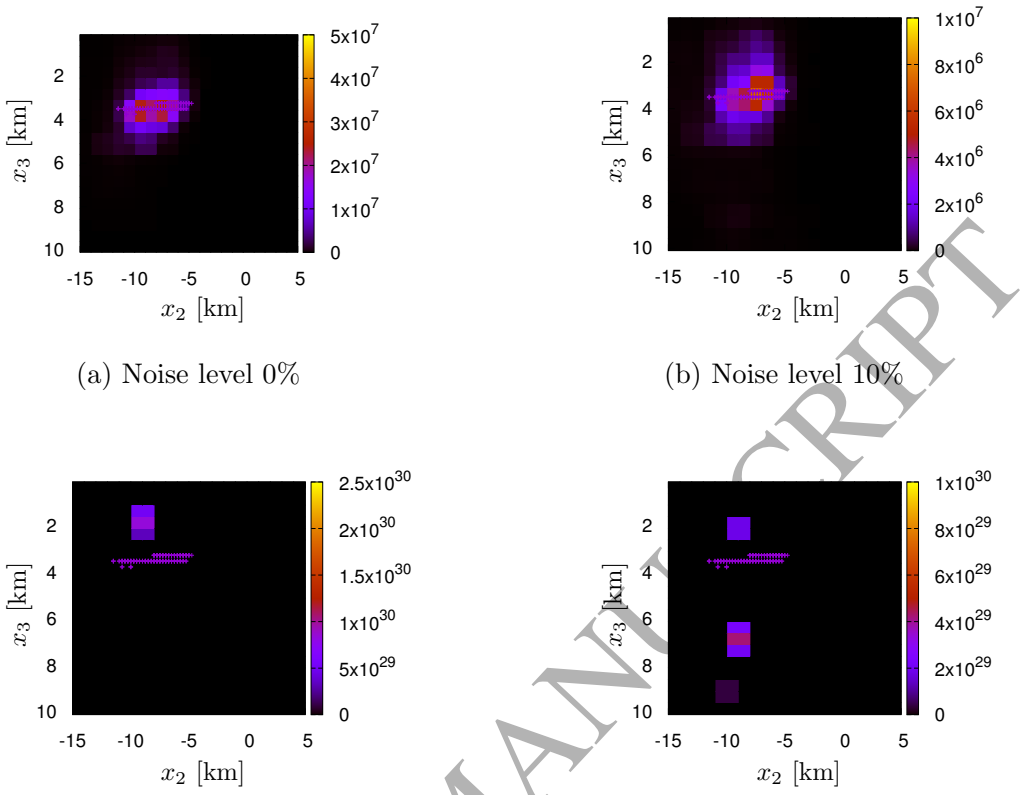

(a) Noise level 0%

(b) Noise level 10%

(c) Noise level 15%

(d) Noise level 20%

Figure 9: Effects of random noise on the accuracy of the reconstruction for the vertical probing plane

3.4 Effect of grid resolution at the free surface

It is desirable to make the number of source and observation points at the free surface as small as possible. In order to examine the effects of a coarser grid resolution at the free surface on the accuracy of the results, we analyzed three cases.

Figure 10 shows the distribution and number of surface gridlines for cases 1, 2, and 3, where the number of source/observation points is 81, 64, and 49, respectively. Figures 11 and 12 show the results of the reconstruction of the scatterers on the horizontal and vertical probing planes, respectively, for progressively coarser surface grids. As can be

seen, the accuracy of the reconstruction of the results decreased as the number of surface points decreased. In spite of this situation, the results are acceptable for cases 1 and 2. For case 3, where the number of grid source/observation points is 49, however, the reconstruction results show excessive deviation from the scatterer locations. In other words, the high-amplitude areas of the indicator functions for case 3 do not describe the locations of the scattering objects.

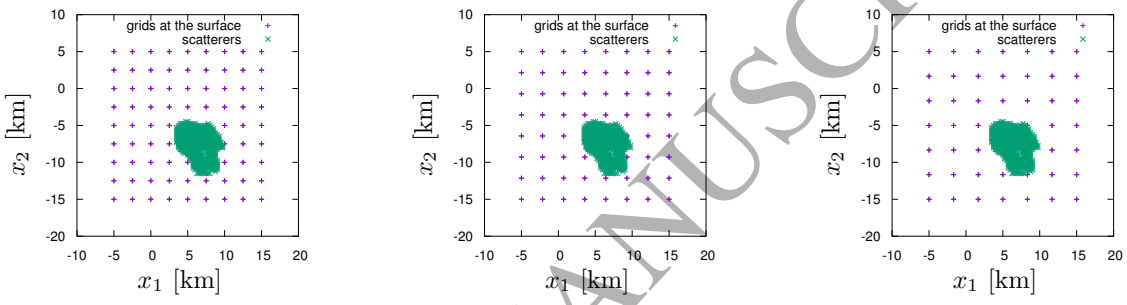

(a) Case 1, 9×9 grid (b) Case 2, 8×8 grid (c) Case 3, 7×7 grid

Figure 10: Analysis model for investigating the effect of the grid resolution at the free surface.

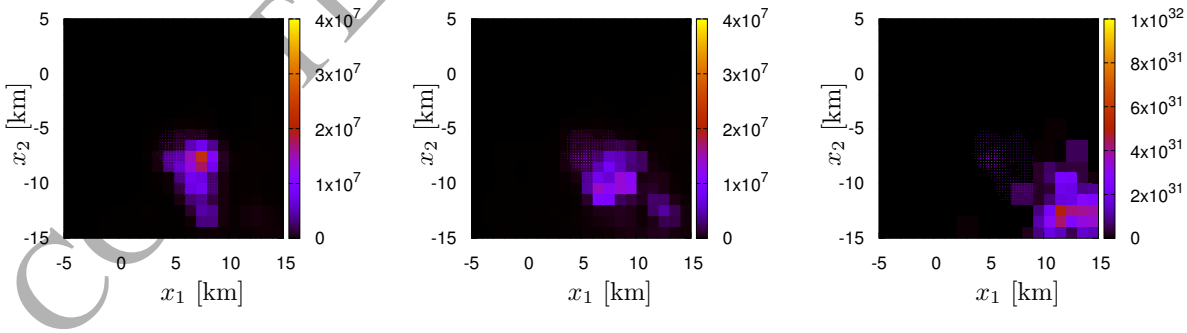

(a) Case 1 (b) Case 2 (c) Case 3

Figure 11: Effects of grid resolution at the free surface on the accuracy of the reconstruction for the horizontal probing plane

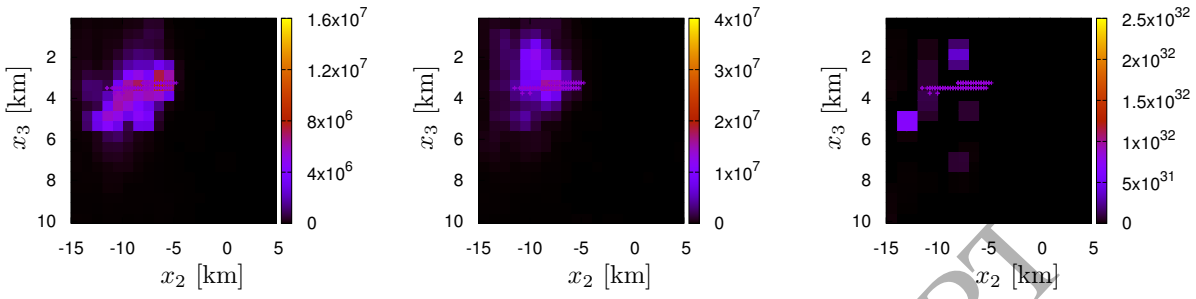

(a) Case 1 (b) Case 2 (c) Case 3

Figure 12: Effect of grid resolution at the free surface on the accuracy of the reconstruction for the vertical probing plane.

3.5 Effect of analyzed frequencies on the accuracy of the reconstruction

As the last set of numerical calculations, we investigate the effect of the analyzed frequency on the accuracy of the reconstruction of the scatterer locations. Figures 13 and 14 show the results of the reconstruction on the horizontal and vertical probing planes, respectively, for analyzed frequencies of 0.5, 1.5, and 2.0 Hz. The high-amplitude areas of the indicator functions on the probing planes are found to accurately reconstruct the locations of the scatterers for all three frequencies. A closer look at the reconstruction results, however, shows that the accuracy in the vertical probing plane decreases slightly as the frequency rises. These results, as well as those for the effects of random noise and surface grid resolution, show recurring difficulties for reconstructing the scatterer locations in the vertical probing plane.

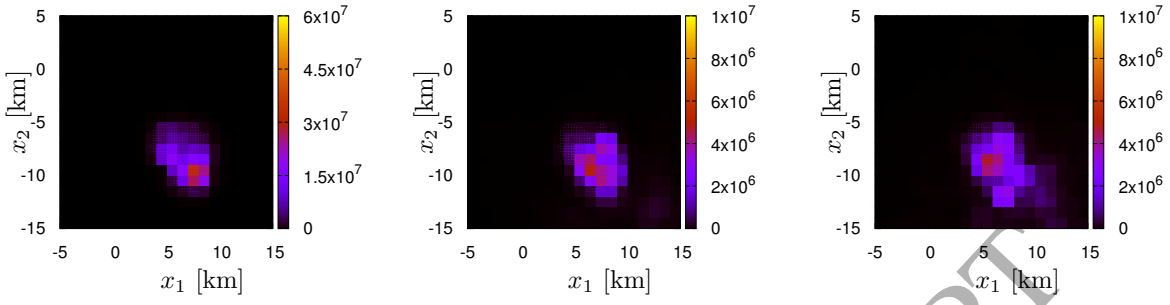

(a) 0.5 Hz (b) 1.5 Hz (c) 2.0 Hz

Figure 13: Effect of the analyzed frequency on the accuracy of the reconstruction for the horizontal probing plane.

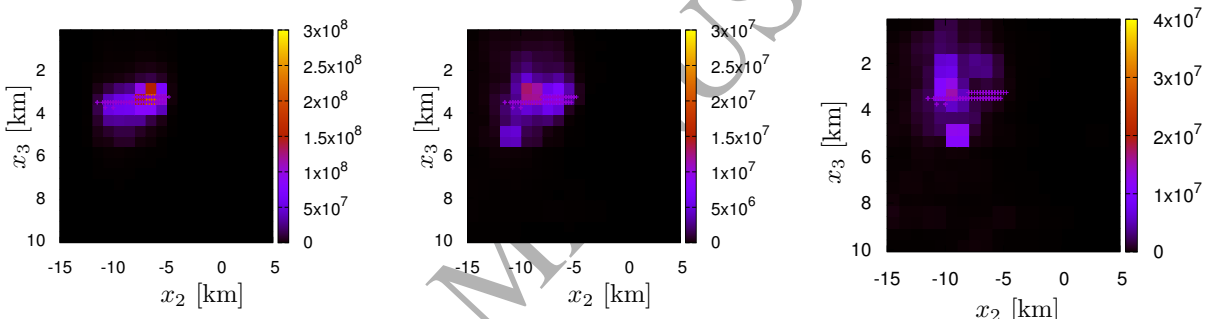

(a) 0.5 Hz (b) 1.5 Hz (c) 2.0 Hz

Figure 14: Effect of the analyzed frequency on the accuracy of the reconstruction for the vertical probing plane.

3.6 Computational costs

Finally, we have to address the computational costs for our proposed method. The near-field operator for the presented numerical examples was derived from the direct wavenumber integral representation of the Green's function. The number of calculation points for the Green's function was based on the product of the number of surface source/observation points and point-like scatterers. In addition, the basis of the kernel of the adjoint of the operator had to be constructed with respect to each probing point. Message Passing

Interface parallel processing was introduced into the numerical calculations by dividing the number of calculation points for the Green's function, as well as the number of probing points, among multiple CPU cores. An Intel Xeon E5-2690, 2.6-GHz CPU used for the numerical calculation. The elapsed time needed for the computation for the analysis model shown in Fig.4 for obtaining the near-field operator and spatial distribution map of the indicator functions on one probing plane was 28 min when 24 cores were used. The number of calculation points for the Green's function and the number of probing points were 121×900 and 441, respectively.

4 Conclusions

This article dealt with reconstruction of the locations of point-like scatterers in an elastic half-space. The introduction of the far-field properties of the Green's function into the near-field operator was the key issue in our formulation. The pseudo projections defined from the asymptotic form of the Green's function played an important role. Due to the use of the pseudo projections, the near-field operator was transformed into a far-field operator that reflected the properties of one type of wave (P, SV, or SH waves). The indicator function was defined from the kernel of the adjoint of the derived far-field operator with respect to each probing point. In the numerical model, the number of point-like scatterers was much larger than the number of source and observation points at the surface, and the set of the point-like scatterers formed a shape of a scattering objects. The effects of random noise and surface grid resolution on the accuracy of the results were also examined. We found that the numerical results supported the validity of our formulation. Future

work will be to carry out the analysis without the Born approximation. Extending the method to an interior transmission scattering problem is also important.

APPENDIX Steepest descent path method for the Green's function for an elastic half-space

A.1 Wavenumber integral representation of the Green's function

The wavenumber integral representation form of the Green's function for an elastic half-space is the starting point of the derivation of the far-field properties of the Green's function. The wavenumber integral representation form itself can be obtained from the Fourier-Hankel transform (Aki and Richards 2002). Based on the procedure (for example, Touhei 2002), the wavenumber integral representation form of the Green's function is expressed as

$$G_{ij}^{S \nwarrow E}(\vec{x}, \vec{y}) = \frac{1}{2\pi} \sum_{m=-1}^{1} C_{ik}(\varphi) \int_0^\infty \xi h_{kl}^{(m)}(\xi : r, \varphi) g_{ln}(\xi : y_3) d\xi \, f_{nj}^{(m)} \quad (\vec{x} \in S, \ \vec{y} \in E) \tag{A.1}$$

where ξ is the radial wavenumber; r and φ are the horizontal range and angle, respectively, between $\vec{x}$ and $\vec{y}$ defined by Fig. 2; m is used for the superscript as well as for summation in the circumferential order number; and $h_{kl}^{(m)}$ is the horizontal wavefunction whose arrays are given as

$$\left[h_{kl}^{(m)}(\xi : r, \varphi) \right] = \begin{bmatrix} 1 & 0 & 0 \\ 0 & \xi^{-1}\partial_r & im(\xi r)^{-1} \\ 0 & im(\xi r)^{-1} & -\xi^{-1}\partial_r \end{bmatrix} J_m(\xi r) \exp(im\varphi) \tag{A.2}$$

where J_m is the first kind of the Bessel function of the m-th order and C_{ik} is the matrix that transforms the cylindrical coordinate system into the Cartesian coordinate system,

for which the components are

$$\Big[C_{ik}(\varphi)\Big] = \begin{bmatrix} 0 & \cos\varphi & -\sin\varphi \\ 0 & \sin\varphi & \cos\varphi \\ 1 & 0 & 0 \end{bmatrix} \tag{A.3}$$

and $f_{nj}^{(m)}$ is given as

$$\Big[f_{nj}^{(m)}\Big] = \begin{cases} \begin{bmatrix} 0 & 0 & 1 \\ 0 & 0 & 0 \\ 0 & 0 & 0 \end{bmatrix} & (m=0) \\ (1/2)\begin{bmatrix} 0 & 0 & 0 \\ 1 & -i & 0 \\ -i & -1 & 0 \end{bmatrix} & (m=1) \\ (1/2)\begin{bmatrix} 0 & 0 & 0 \\ -1 & -i & 0 \\ -i & 1 & 0 \end{bmatrix} & (m=-1) \end{cases} \tag{A.4}$$

In addition, $g_{ln}(\xi, y_3)$ is the Green's function in the wavenumber domain, which is decomposed into

$$\Big[g_{ln}(\xi,y_3)\Big] = \frac{e^{-\gamma y_3}}{\gamma}\Big[g_{ln}^{(\alpha)}(\xi)\Big] + \frac{e^{-\nu y_3}}{\nu}\Big[g_{ln}^{(\beta_V)}(\xi)\Big] + \frac{e^{-\nu y_3}}{\nu}\Big[g_{ln}^{(\beta_H)}(\xi)\Big] \tag{A.5}$$

where

$$\begin{aligned} \gamma &= \sqrt{\xi^2 - \xi_\alpha^2} \\ \nu &= \sqrt{\xi^2 - \xi_\beta^2} \end{aligned} \tag{A.6}$$

and $[g_{ln}^{(\alpha)}]$, $[g_{ln}^{(\beta_V)}]$, and $[g_{ln}^{(\beta_H)}]$ are functions of the wavenumber in the form of matrices expressing the contributions to the P, SV, and SH waves, respectively. The arrays for the functions are as follows:

$$\begin{aligned} \Big[g_{ln}^{(\alpha)}(\xi)\Big] &= \frac{1}{\mu F(\xi)}\begin{bmatrix} \gamma^2(\xi^2+\nu^2) & -\xi\gamma(\xi^2+\nu^2) & 0 \\ \xi\gamma^2\nu & -2\nu\gamma\xi^2 & 0 \\ 0 & 0 & 0 \end{bmatrix} \\ \Big[g_{ln}^{(\beta_V)}(\xi)\Big] &= \frac{1}{\mu F(\xi)}\begin{bmatrix} -2\xi^2\gamma\nu & 2\xi\gamma\nu & 0 \\ -\xi\nu^2(\xi^2+\nu^2) & \nu^2(\xi^2+\nu^2) & 0 \\ 0 & 0 & 0 \end{bmatrix} \\ \Big[g_{ln}^{(\beta_H)}(\xi)\Big] &= \frac{1}{\mu}\begin{bmatrix} 0 & 0 & 0 \\ 0 & 0 & 0 \\ 0 & 0 & 1 \end{bmatrix} \end{aligned} \tag{A.7}$$

where $F(\xi)$ is the Rayleigh function defined by

$$F(\xi) \;=\; (2\xi^2 - \xi_\beta^2)^2 - 4\xi^2\gamma\nu \tag{A.8}$$

A.2 Application of the steepest descent path method

Application of the steepest descent path method to the direct wavenumber integral representation of the Green's function is the key for the derivation of the far-field properties of the Green's function. First, we modify Eq. (A.1) as follows:

$$G_{ij}^{S\nwarrow E}(\vec{x},\vec{y}) \;=\; \frac{1}{4\pi}\sum_{m=-1}^{1} C_{ik}(\varphi)\int_{-\infty}^{\infty} \xi h_{kl}^{(m(1))}(\xi : r,\varphi) g_{ln}(\xi : y_3) d\xi \; f_{nj}^{(m)} \tag{A.9}$$

where

$$\Big[h_{kl}^{(m(1))}(\xi : r,\varphi)\Big] = \begin{bmatrix} 1 & 0 & 0 \\ 0 & \xi^{-1}\partial_r & im(\xi r)^{-1} \\ 0 & im(\xi r)^{-1} & -\xi^{-1}\partial_r \end{bmatrix} H_m^{(1)}(\xi r)\exp(im\varphi) \tag{A.10}$$

In the above expression, the following properties of the Bessel functions are used:

$$\begin{aligned} J_m(\xi r) &= \frac{1}{2}\Big[H_m^{(1)}(\xi r) + H_m^{(2)}(\xi r)\Big] \\ H_m^{(2)}(-\xi r) &= -H_m^{(2)}(\xi r), \quad (m = 0, \pm 2) \\ H_m^{(1)}(-\xi r) &= H_m^{(2)}(\xi r), \quad (m = \pm 1) \end{aligned} \tag{A.11}$$

where $H_m^{(\tau)}(\cdot)$ is the Hankel function of order m. Now, let

$$\eta_m = \pi m/2 \tag{A.12}$$

then, the asymptotic behavior of the horizontal wavefunction becomes

$$h_{kl}^{(m(1))}(\xi, r, \varphi) = \sqrt{\frac{2}{\pi\xi r}} e^{i\xi r} e^{im\varphi} e^{-i\pi/4}\, \hat{h}_{kl}^{(m)} + O(r^{-3/2}) \tag{A.13}$$

where

$$\left[\hat{h}_{kl}^{(m)}\right] = \begin{bmatrix} e^{-i\eta_m} & 0 & 0 \\ 0 & (1/2)[e^{-i\eta_{m-1}} - e^{-i\eta_{m+1}}] & (i/2)[e^{-i\eta_{m-1}} + e^{-i\eta_{m+1}}] \\ 0 & (i/2)[e^{-i\eta_{m-1}} + e^{-i\eta_{m+1}}] & -(1/2)[e^{-i\eta_{m-1}} - e^{-i\eta_{m+1}}] \end{bmatrix} \quad \text{(A.14)}$$

At this point, we can divide the Green's function into three components based on the contributions from the P, SV, and SH waves as follows:

$$G_{ij}^{S\nwarrow E}(\vec{x},\vec{y}) = G_{ij}^{S\nwarrow E(\alpha)}(\vec{x},\vec{y}) + G_{ij}^{E\nwarrow E(\beta_V)}(\vec{x},\vec{y}) + G_{ij}^{E\nwarrow E(\beta_H)}(\vec{x},\vec{y}) \quad \text{(A.15)}$$

where

$$\begin{aligned} G_{ij}^{S\nwarrow E(\alpha)}(\vec{x},\vec{y}) &= \frac{1}{4\pi}\sqrt{\frac{2}{\pi r}}\sum_{m=-1}^{1} C_{ik}(\varphi)e^{im\varphi} \\ &\quad \times \int_{-\infty}^{\infty} \frac{\sqrt{\xi}}{\gamma}\exp(i\xi r - \gamma y_3 - i\pi/4)\hat{h}_{kl}^{(m)} g_{ln}^{(\alpha)}(\xi)\, d\xi\, f_{nj}^{(m)} \\ &\quad + O(r^{-3/2}) \end{aligned} \quad \text{(A.16)}$$

$$\begin{aligned} G_{ij}^{S\nwarrow E(\beta_V)}(\vec{x},\vec{y}) &= \frac{1}{4\pi}\sqrt{\frac{2}{\pi r}}\sum_{m=-1}^{1} C_{ik}(\varphi)e^{im\varphi} \\ &\quad \times \int_{-\infty}^{\infty} \frac{\sqrt{\xi}}{\nu}\exp(i\xi r - \nu y_3 - i\pi/4)\, \hat{h}_{kl}^{(m)} g_{ln}^{(\beta_V)}(\xi)\, d\xi\, f_{nj}^{(m)} \\ &\quad + O(r^{-3/2}) \end{aligned} \quad \text{(A.17)}$$

$$\begin{aligned} G_{ij}^{S\nwarrow E(\beta_H)}(\vec{x},\vec{y}) &= \frac{1}{4\pi}\sqrt{\frac{2}{\pi r}}\sum_{m=-1}^{1} C_{ik}(\varphi)e^{im\varphi} \\ &\quad \times \int_{-\infty}^{\infty} \frac{\sqrt{\xi}}{\nu}\exp(i\xi r - \nu y_3 - i\pi/4)\, \hat{h}_{kl}^{(m)} g_{ln}^{(\beta_H)}(\xi)\, d\xi\, f_{nj}^{(m)} \\ &\quad + O(r^{-3/2}) \end{aligned} \quad \text{(A.18)}$$

The path of the wavenumber integral in the complex wavenumber plane for the application of the steepest descent path method is shown in Fig. A.1, in which the saddle point is denoted by the blue point on the real axis. In the following discussion, we employ

the notation $\xi_{s\alpha}$ and $\xi_{s\beta}$ for the saddle points of the P and S waves, respectively. The relationship between the saddle point and the P and S wavenumber is

$$\begin{aligned} \xi_{s\alpha} &= \xi_\alpha \sin\theta \\ \xi_{s\beta} &= \xi_\beta \sin\theta \end{aligned} \tag{A.19}$$

where θ is determined by the relative locations of $\vec{x}$ and $\vec{y}$, which are explained by Fig. 2 in the main text of this article. The steepest descent paths are also described by the blue lines in Fig. A.1. Note that there is a case where $\xi_{s\beta} > \xi_\alpha$. In this case, the integral path B around the branch point ξ_α is required, as shown in case 2 in Fig. A.1. In addition, we have to take into account the contribution from the Rayleigh pole. It is known that the Green's function is expressed by the contributions from the residue term related to the Rayleigh pole, steepest descent path, and branch line integral. When the region of E is deep enough from the free surface, the contribution from the Rayleigh wave mode to the Green's function $G_{ij}^{S\nwarrow E}$ can be ignored, since the Rayleigh wave mode decays exponentially with depth. Furthermore, the contribution from the branch line integral shows a geometrical decay of $O(R^2)$ when $R = |\vec{x} - \vec{y}|$. As a result, the Green's function can be approximated by the contribution from the steepest descent path that shows the geometrical decaying $O(R^{-1})$ becoming

$$\begin{aligned} G_{ij}^{S\nwarrow E}(\vec{x},\vec{y}) = & \frac{e^{i\xi_\alpha R}}{4\pi R} D_{ij}^{S\nwarrow E(\infty,\alpha)}(\theta,\varphi) + \frac{e^{i\xi_\beta R}}{4\pi R} D_{ij}^{S\nwarrow E(\infty,\beta_V)}(\theta,\varphi) + \frac{e^{i\xi_\beta R}}{4\pi R} D_{ij}^{S\nwarrow E(\infty,\beta_H)}(\theta,\varphi) \\ & + O(R^{-2}) \end{aligned} \tag{A.20}$$

where

$$
\begin{aligned}
D_{ij}^{S\nwarrow E(\infty,\alpha)}(\theta,\varphi) &= 2C_{ik}(\varphi)\sum_{m=-1}^{1} e^{im\varphi}\left[\hat{h}_{kl}^{(m)} g_{ln}^{(\alpha)}(\xi)\right]_{\xi=\xi_\alpha \sin\theta} f_{nl}^{(m)} \\
D_{ij}^{S\nwarrow E(\infty,\beta_V)}(\theta,\varphi) &= 2C_{ik}(\varphi)\sum_{m=-1}^{1} e^{im\varphi}\left[\hat{h}_{kl}^{(m)} g_{ln}^{(\beta_V)}(\xi)\right]_{\xi=\xi_\beta \sin\theta} f_{nl}^{(m)} \\
D_{ij}^{S\nwarrow E(\infty,\beta_H)}(\theta,\varphi) &= 2C_{ik}(\varphi)\sum_{m=-1}^{1} e^{im\varphi}\left[\hat{h}_{kl}^{(m)} g_{ln}^{(\beta_H)}(\xi)\right]_{\xi=\xi_\beta \sin\theta} f_{nl}^{(m)}
\end{aligned}
\tag{A.21}
$$

and θ is explained in Fig. 2 and defined by

$$
\theta = \sin^{-1}(y_3/R) \tag{A.22}
$$

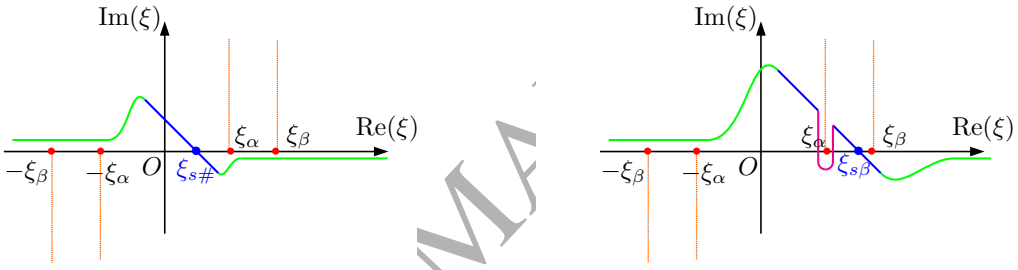

(a) Path of integral (case 1) (b) Path of integral (case 2)

Figure A.1: Steepest descent paths. The path for case 1 denotes the P and S waves when $\xi_{s\beta} < \xi_\alpha$. The path for case 2 denotes the S wave when $\xi_\alpha < \xi_{s\beta}$. The branch line integral for the S-P wave is required for case 2.

A remaining task in this **Appendix** is to examine the accuracy of the asymptotic form of the Green's function shown in Eq. (A.20). Figure A.2 is the model for the verification, in which a buried point source is located at the x_3 axis and the Green's function is compared at the free surface along the x_1 axis. The direction of the excitation force is vertical, so the responses are also calculated for the vertical direction. The P and S wave velocities are 2 km/s and 1 km/s, respectively, and the mass density is 2 g/cm^3. In addition, the excitation frequency is 1 Hz and the force amplitude is 10^7 kN.

Figure A.3 shows a comparison between the Green's function calculated from the direct wavenumber integral representation and its asymptotic form shown in Eq. (A.20). It is found from Fig. A.3 that the both results show almost good agreement especially in the farfield range. As the depth of the point source increases, the agreements are also found to improve. These results reflect the properties of the asymptotic form of the Green's function. Note that the depth of the point-like scatterers in numerical examples presented in the article are around from 3 km to 5 km. Therefore, the asymptotic form of the Green's function presented in the range of the numerical calculations well approximate the Green's function calculated by the direct wavenumber integral.

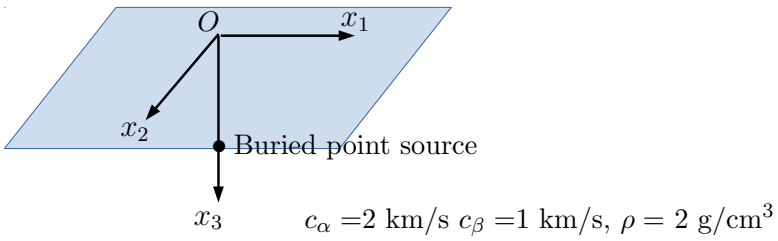

Figure A.2: Buried point source model for examining the accuracy of the asymptotic form of the Green's function.

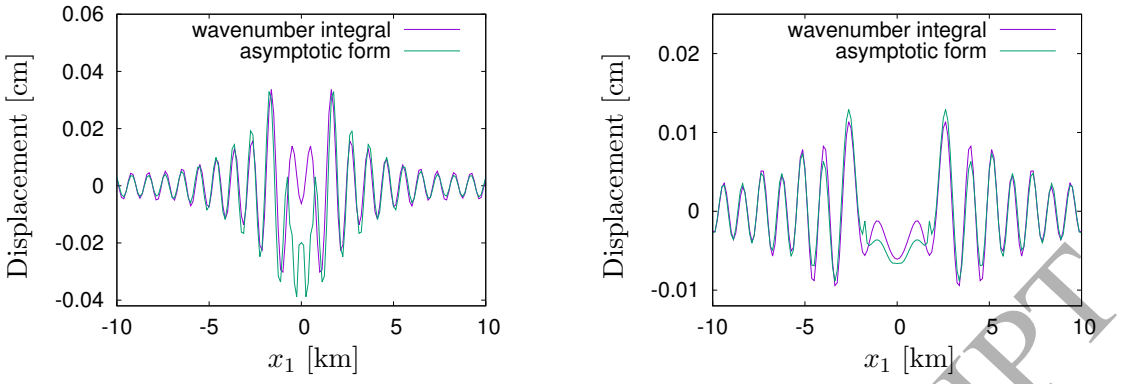

(a) Source depth = 1 km (b) Source depth = 3 km

Figure A.3: Comparison of the Green's function calculated by the wavenumber integral with its asymptotic form. The vertical displacements due to the vertical excitation are compared for two depths.

REFERENCES

Abubakar, A., Pan, G., Li, M., Zhang, L. Habashy, T.M., and van den Berg, P.M, Three-dimensional seismic full-waveform inversion using the finite-difference contrast source inversion method, Geophysical prospecting, Special Issue: Modelling Methods for Geophysical Imaging: Trends and Perspective, Vol. 59, Issue 5, pp. 874-888, 2011.

Aki, K., and Richards, P.G., 1980. Quantitative Seismology, Theory and Methods., W. H. Freeman and Company.

Baganas, K., Guzina, B.B, Charalambopoulos, A. (2006) A linear sampling method for the inverse transmission problem in near-field elastodynamics, Inverse problems, 22, 1835-1853.

Colton, D. and Kirsch, A. (1996) A simple method for solving inverse scattering problems

in the resonance region, Inverse problems, 12, 383-393.

Colton, D. and Kress, R., 1998. Inverse acoustic and electromagnetic scattering theory, Berlin, Springer.

Fata, S.N. and Guzina, B.B., 2004. A linear sampling method for near-field inverse problems in elastodynamics, Inverse Problems, 20, 713-736.

Gintides, D., Sini, M. and Thành, N.T., Detection of point-like scatterers using one type of scattered elastic waves, Journal of computational and applied mathematics, vol. 236, pp. 2137-2145, 2012

Guzina, B.B. and Madyarov, A.I., 2007, A linear sampling approach to inverse elastic scattering in piecewise-homogeneous domains, Inverse Problems, 23, 1467-1493.

Kirsch, A. 2011, The factorization method for inverse problems, Newton Institute, `http://www.newton.ac.uk/files/seminar/20110728090009451-152765.pdf`

Pelekanos, G., Abubakar, A. and van den Berg, P.M., 2004. Contrast source inversion methods in Elastodynamics, J. Acoust. Soc. Am, 114, 2825-2834

Pourahmadian1, F., Guzina, B.B. and Haddar, H.: Generalized linear sampling method for elastic-wave sensing of heterogeneous fractures Inverse Problems, Volume 33, Number 5, 2017.

Romdhane, A., Grandjean, G., Brossier, R., Réjiba, F., Operto, S., and Virieux, J. 2011, Shallow structures characterization by 2d elastic waveform inversion, Geophysics, 76(3), R81-R93.

Terumi Touhei, 2003, Analysis of scattering waves in an elastic layered medium by means of the complete eigenfunction expansion form of the Green's function, Int.J. Solids and Struct, 40, pp. 3347-3377

Touhei, T. Fukushiro, Y. and Tanaka, T, 2015. A linear sampling method for detecting fluctuations for an elastic half-space, International Journal of Solids and Structures 72, 26-37.